Downlink Analysis and Evaluation of Multi-Beam LEO Satellite Communication in Shadowed Rician Channels

Eunsun Kim, *Student Member, IEEE,* Ian P. Roberts, *Member, IEEE,*
and Jeffrey G. Andrews, *Fellow, IEEE*

***Abstract*—A multi-beam low-earth orbit (LEO) satellite delivers widespread coverage by forming spot beams that tessellate cells on the surface of the Earth. In doing so, co-channel interference manifests between cells when reusing frequency spectrum across spot beams. To permit forecasting of such multi-beam satellite communication system performance, this work characterizes desired and interference signal powers under the Shadowed Rician (SR) sky-to-ground channel model, along with SNR, INR, SIR, and SINR. Specifically, we present a framework for analyzing system performance by capitalizing on the fact that the desired and interfering signals travel along almost the same path in such multi-beam satellite systems. We then introduce a minor approximation on the fading order of SR channels that significantly simplifies the probability distribution function and cumulative distribution function of these quantities and facilitates performance analyses of LEO satellite systems. We conclude this paper with an evaluation of multi-beam LEO satellite communication in SR channels of varying intensity with shadowing parameters fitted from existing measurements. Our numerical results highlight the effect satellite elevation angle has on SNR, INR, and SINR, which brings attention to the variability in system state and potential performance as a satellite traverses across the sky along its orbit.**

I. INTRODUCTION

LOW-EARTH ORBIT (LEO) satellite communication systems are experiencing a renaissance. Deployment costs have dropped dramatically due to new launch technologies, both enabling and being enabled by ongoing mass satellite deployments such as SpaceX's Starlink [2] and Amazon's Project Kuiper [3]. Efforts such as these are slated to deploy constellations comprised of thousands or even tens of thousands of LEO satellites, targeted to deliver high-capacity broadband connectivity to un/under-served communities, as well as supplement existing terrestrial wireless services in better-served areas. A single LEO satellite can deliver broad coverage by tessellating multiple spot beams on the ground, whose collective footprint may have a diameter on the order of tens or hundreds of kilometers. The orbiting nature of LEO satellite constellations along with characteristics of sky-to-ground propagation poses link-level and network-level challenges unseen in terrestrial cellular networks. The success of emerging LEO satellite communication systems and their role in next-generation connectivity will rely on accurately evaluating their potential through practically-sound analysis and simulation.

A. Background and Prior Work

Having multiple antennas onboard a single satellite allows it to form multiple high-gain spot beams simultaneously and is a promising route to satisfy the demand for high data rates and provide broad coverage, both in LEO and geostationary satellite systems [2]–[6]. The formation of multiple beams, however, leads to co-channel interference that can degrade downlink quality of service [7], [8] when these beams use the same frequency resources. Mitigating this co-channel interference in multi-beam satellite systems has been studied extensively, with proposed solutions including less aggressive frequency reuse, strategic beam design, and interference cancellation [7]–[10].

As a satellite traverses across the sky along its orbit, the spot beam patterns observed on the ground distort—even when correcting its beams' steering directions along the way. This is attributed to the fact that a spot beam's radiation pattern projects differently onto the surface of the Earth depending on satellite position. As a result, the elevation angle of a satellite relative to a ground user dictates the quality of service it delivers. These factors were less of a concern in geostationary satellite systems due to their near static relative positioning, but the fast orbital speeds of LEO satellites magnify the time-varying nature of these effects, given that a ground user is in view of a particular satellite for mere minutes at most [11]–[13].

In addition to the orbiting nature of satellites, sky-to-ground propagation also plays a central role in dictating the performance of LEO satellite systems. The Shadowed Rician (SR) model [14] has been adopted widely in the literature [15]–[20] to model the satellite channel, as it aligns well with measurements and offers a closed-form probability distribution function (PDF) and cumulative distribution function (CDF)

Manuscript received January 27, 2023; revised June 29, 2023; accepted September 3, 2023. This work is supported by the affiliates of 6G@UT and by the Truchard Family Endowed Chair in Engineering. The work of I. P. Roberts was supported in part by the National Science Foundation under Grant 1610403. Corresponding author: Eunsun Kim (esunkim@utexas.edu).

E. Kim and J. G. Andrews are with the 6G@UT Research Center, Wireless Networking and Communications Group, University of Texas at Austin, Austin, TX 78712 USA.

I. P. Roberts was with the University of Texas at Austin; he is now with the Department of Electrical and Computer Engineering, UCLA, Los Angeles, CA 90095 USA.

This work is an extension of our prior work [1].

[14]. In this SR channel model, line-of-sight (LOS) and non-line-of-sight (NLOS) propagation are combined in a Rician fashion, where the magnitude of each component randomly fluctuates. With the magnitude of the channel modeled as an SR random variable, the resulting signal power is a Squared Shadowed Rician (SSR) random variable, whose PDF and CDF were derived in [17], [18], along with that for the sum of SSR random variables. However, these expressions involve infinite power series and special functions making them quite complex.

In this work, we characterize key performance quantities of a multi-beam satellite system, such as desired and interference signal powers. It is important to recognize that the interference inflicted by neighboring spot beams formed by a single satellite propagates along the same path as its desired signals to a ground user. In other words, in this multi-beam system, interference is fully correlated with desired receive signals. As a result, the collective interference from the satellite can be modeled as a sum of correlated SSR random variables under the SR channel. Studies on statistics of the sum of SSR random variables typically consider these random variables independent [15], [17], [19], as these studies intend to characterize the sum of desired signal powers when leveraging transmit diversity. The work of [17] includes studies on the sum of correlated SSR random variables to characterize the total received signal power when only LOS components are correlated and NLOS components are independent. While this assumption simplifies mathematical expressions, its physical interpretation is not necessarily clear, making its relevance uncertain in real systems.

Existing work [8], [15]–[24] has evaluated multi-beam satellite communication systems but does not account for a number of important practical considerations. The work of [8], for instance, does not account for the distorted beam shape when a satellite is not directly overhead, instead assuming perfectly circular coverage on the ground regardless of elevation angle. In addition, shadowing has not been incorporated in [21], which has instead assumed channels to be unfaded LOS channels. Multi-beam satellite systems under the SR channel are studied in [15], [17], [19], where the sum of independent SSR random variables is derived, while [22]–[24] assess throughput and coverage performance of LEO satellite systems but ignore interference between spot beams.

To the best of our knowledge, no existing work analyzes multi-beam satellite systems under SR channels, taking into account satellite elevation, in which the desired and interfering signals are fully correlated as they propagate from the satellite to a ground user. All this motivates the need to appropriately evaluate multi-beam LEO systems while accounting for practical factors that play a central role in determining system performance.

B. Contributions

A novel analysis of multi-beam LEO satellite systems. We recognize that signals from a multi-beam satellite to a target user are fully correlated rather than independent since they traverse along the same channel, and thus the downlink desired and interference signals to the target user are also fully correlated. We leverage this to characterize signal-to-noise ratio (SNR), interference-to-noise ratio (INR), signal-to-interference ratio (SIR), and signal-to-interference-plus-noise ratio (SINR) of the system under SR channels. In doing so, we derive relations between linearly-related SR and SSR random variables. To facilitate this characterization, we show that rounding the fading order of an SR channel to an integer can remove infinite series from expressions for its PDF and CDF, which in turn yields closed-form statistics, such as expectation. We show that this rounding has virtually no effect on the fading distribution and, as an added benefit, simplifies numerical realization by removing the presence of infinite series.

Comprehensive performance evaluation of multi-beam LEO satellite systems. Through simulation, we incorporate the effects of multi-beam interference, elevation angle, SR channels, and frequency reuse to investigate their impact on SNR, INR, and SINR. To appropriately model a variety of SR channels, we employ three shadowing levels—light, average, and heavy—whose statistical parameters have been fitted from measurements [14], [25], [26]. We show that the system can be heavily interference-limited or noise-limited, depending on elevation angle and shadowing conditions, but frequency reuse can be a reliable route to reduce interference. Considering the orbital speed of LEO satellites, the system can swing from interference-limited to noise-limited and back to interference-limited over the course of a few minutes as the satellite traverses across the sky. This, along with other results from our performance evaluation, can drive design decisions pertaining to cell planning, beam design, and handover and can motivate a variety of future work.

C. Organization

In Section II, we provide the system model with a brief introduction on the SR channel model. In Section III, we characterize performance metrics based on this system model. In Section IV, we introduce a useful approximation on the fading order of SR random variables. We provide a comprehensive performance evaluation of multi-beam LEO satellite systems under the SR channel in Section V. We conclude this paper in Section VI.

II. SYSTEM MODEL

We consider a single LEO satellite serving multiple users on the ground. The satellite is equipped with multiple phased array or dish antennas to simultaneously form multiple spot beams. The coverage provided by each spot beam establishes a *cell* on the surface of the Earth to provide wireless connectivity to users on the ground. As illustrated in Fig. 1, cells are tessellated by steering spot beams to different points on the Earth, forming the satellite's total coverage *footprint*. The contribution in this work is characterizing the *multi-beam interference* that manifests between spot beams originating from a single satellite. Other sources of interference, such as those from other satellites or terrestrial sources, could be

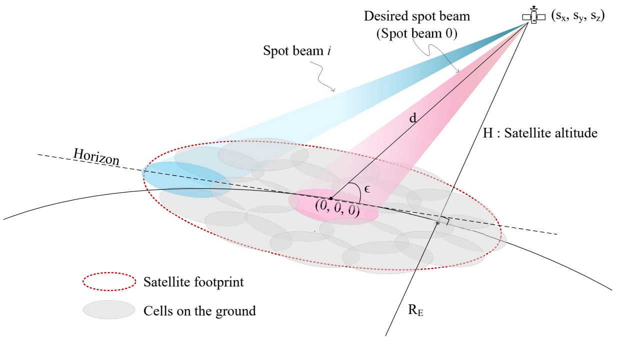

Fig. 1. A LEO satellite located at a position (s_x, s_y, s_z) with altitude H and elevation angle ϵ delivers downlink to ground users with multiple onboard transmitters, each of which steers a spot beam to illuminate a cell on the ground, collectively comprising the satellite footprint. In addition to receiving desired downlink signals, ground users also incur interference from neighboring spot beams.

considered supplemental to this work and are left to future studies.

At a given instant, suppose the satellite is located at a position (s_x, s_y, s_z) in Cartesian coordinates relative to some origin on the surface of the Earth, as illustrated in Fig. 1, which can be written as

$$(s_x, s_y, s_z) = (d \cos\epsilon \cos\Phi, d\cos\epsilon \sin\Phi, d\sin\epsilon), \tag{1}$$

where ϵ and Φ are the elevation and azimuth angles of the satellite, respectively, and d is the absolute distance (or *slant distance*) to the satellite. The slant distance d can be expressed in terms of the satellite altitude H and its elevation angle ϵ as

$$d = \sqrt{R_{\mathrm{E}}^2 \sin^2\epsilon + H^2 + 2HR_{\mathrm{E}}} - R_{\mathrm{E}} \sin\epsilon, \tag{2}$$

where $R_{\mathrm{E}} \approx 6,378$ km is the radius of the Earth.

Let N_{B} be the number of spot beams formed by the satellite, where each spot beam is driven by a dedicated transmitter onboard the satellite with total conducted transmit power P_{tx}. We denote $G_i(\phi, \theta)$ as the gain of the i-th spot beam toward some azimuth ϕ and elevation θ relative to its steering direction, where $i = 1, \ldots, N_{\mathrm{B}}$. Each spot beam is steered toward the center of the cell it serves, as illustrated in Fig. 1, which is often practically more manageable than user-specific beamforming.

Let x_i be the transmitted symbol from the i-th transmitter where $\mathbb{E}\left[|x_i|^2\right] = 1$. Transmissions by each spot beam will inflict interference onto ground users served by the other $N_{\mathrm{B}} - 1$ beams, since practical beam patterns naturally leak energy in undesired directions. Given the overwhelming distance between the satellite and a ground user relative to the separation between onboard antennas, a desired signal and the corresponding $N_{\mathrm{B}} - 1$ interference signals experience approximately the same propagation channel h and same path loss PL to a target user. As such, we can write the received symbol of the user being served by the i-th spot beam as

$$y_i = \underbrace{\sqrt{P_{\mathrm{tx}} \cdot \mathrm{PL}^{-1} \cdot G_i(\phi_i, \theta_i)} \cdot h \cdot x_i}_{\text{desired signal}} + \underbrace{\sum_{j=1, j\neq i}^{N_{\mathrm{B}}} \sqrt{P_{\mathrm{tx}} \cdot \mathrm{PL}^{-1} \cdot G_j(\phi_j, \theta_j)} \cdot h \cdot x_j + n_i}_{\text{collective spot-beam interference}}, \tag{3}$$

where h is the sky-to-ground propagation channel and $n_i \sim \mathcal{N}_{\mathbb{C}}\left(0, \sigma_{\mathrm{n}}^2\right)$ is additive noise. Here, (ϕ_i, θ_i) is the relative azimuth-elevation of the ground user relative to the steering direction of the i-th spot beam. Consequently, the degree of interference incurred by a ground user depends on its location and the steering directions of the N_{B} spot beams (i.e., the cell placement) along with the spot beam patterns. Receive antenna gain can be incorporated straightforwardly, but for the sake of conciseness, we omit it since it acts identically on a desired signal and interference.

We model sky-to-ground propagation with the SR channel model [14], where the channel magnitude is an SR random variable distributed as

$$|h| \sim \mathsf{SR}(b, m, \Omega). \tag{4}$$

Based on actual measurements [25], [26], the SR channel model accurately captures both LOS and NLOS propagation in a Rician fashion and incorporates random fluctuations of each, caused by obstructions such as buildings, trees, and vegetation [14]. The three parameters of the SR channel model can be summarized as:

- Ω being the average power of the LOS component;
- $2b$ being the average power of the NLOS component;
- m being the fading order dictating the general shape of the distribution.

The PDF of $|h|$ is defined as in (5), where ${}_1\mathcal{F}_1(\cdot,\cdot,\cdot)$ is the confluent hypergeometric function [27], namely

$${}_1\mathcal{F}_1(a, b, x) = \sum_{n=0}^{\infty} \frac{(a)_n}{n!(b)_n} x^n, \tag{6}$$

with $(a)_n \triangleq a(a+1)\cdots(a+n-1)$ denoting the Pochhammer symbol [28]. With this presented downlink system model, we derive and characterize key performance metrics in the next section.

III. CHARACTERIZING PERFORMANCE IN SHADOWED RICIAN CHANNELS

Using the system model presented in the previous section, we aim to characterize key performance metrics of the system, most notably SNR, SIR, INR, and SINR, which can drive system design, as we will highlight herein. In doing so, we establish several relations between linearly-related SR random variables, allowing us to describe these performance metrics in terms of the system's SR channel parameters.

$$f_{|h|}(x;b,m,\Omega)=\frac{x}{b}\left(\frac{2bm}{2bm+\Omega}\right)^{m}\exp\left(-\frac{x^2}{2b}\right){}_1\mathcal{F}_1\left(m,1,\frac{\Omega}{2b(2bm+\Omega)}x^2\right) \tag{5}$$

$$f_{|h|^2}(y;b,m,\Omega)=\frac{1}{2b}\left(\frac{2bm}{2bm+\Omega}\right)^{m}\exp\left(-\frac{y}{2b}\right){}_1\mathcal{F}_1\left(m,1,\frac{\Omega}{2b(2bm+\Omega)}y\right) \tag{8}$$

$$F_{|h|^2}(y;b,m,\Omega)=\frac{y}{2b}\left(\frac{2bm}{2bm+\Omega}\right)^{m}\Phi_2\left(1-m,m;2;-\frac{1}{2b}y,-\frac{m}{2bm+\Omega}y\right) \tag{9}$$

A. Desired Signal Power and SNR

With the magnitude of the channel modeled as an SR random variable $|h| \sim \mathsf{SR}(b,m,\Omega)$, the channel power gain follows an SSR distribution as

$$|h|^2 \sim \mathsf{SSR}(b,m,\Omega), \tag{7}$$

with its PDF given as (8) [14]. Its CDF is quite involved but can be expressed as in (9) [29], where Φ_2 is the bivariate confluent hypergeometric function defined as [28], [30]

$$\Phi_2(a,a';c;w,z)=\sum_{k=0}^{\infty}\frac{(a)_k}{k!(c)_k}w^k{}_1\mathcal{F}_1(a',c+k,z). \tag{10}$$

From (3), we can write the power of the desired signal received by a ground user served by the i-th spot beam as

$$P_{\mathrm{des}}=P_{\mathrm{tx}}\cdot\mathrm{PL}^{-1}\cdot G_i(\phi_i,\theta_i)\cdot|h|^2, \tag{11}$$

which itself is a random variable linearly related to $|h|^2$, since all other terms are deterministic for a given ground user location. To describe P_{des}, we introduce the following theorem to establish the relationship between SR and SSR random variables.

Theorem 1. *If $X \sim \mathsf{SR}(b,m,\Omega)$ and $Y = k\cdot X^2$ for $k>0$, then*

$$Y \sim \mathsf{SSR}(k\cdot b,m,k\cdot\Omega). \tag{12}$$

Proof. See Appendix A. □

Corollary 1.1. *Two SSR random variables $Y_1 \sim \mathsf{SSR}(b_1,m_1,\Omega_1)$ and $Y_2 \sim \mathsf{SSR}(b_2,m_2,\Omega_2)$ are linearly related as $Y_1 = k\cdot Y_2$ for $k>0$ if*

$$m_1=m_2 \quad \textit{and} \quad \frac{b_1}{b_2}=\frac{\Omega_1}{\Omega_2}=k. \tag{13}$$

Corollary 1.1 provides a clear insight on linearly-related SSR random variables and the relationship of their parameters. Suppose we have two SSR random variables Y_1 and Y_2 which are linearly scaled as $Y_1 = k\cdot Y_2$. Then, their LOS and NLOS parameters are also exactly scaled by k (i.e., $b_1 = k\cdot b_2$ and $\Omega_1 = k\cdot\Omega_2$) whereas the fading order remains the same (i.e., $m_1 = m_2$). In other words, if the ratio of the LOS and NLOS components are equal and they have the same fading order m, then Y_1 and Y_2 share a common distribution function.

With the channel $|h| \sim \mathsf{SR}(b,m,\Omega)$ distributed as an SR random variable, Theorem 1 states that P_{des} is an SSR random variable that can be inferred directly as

$$P_{\mathrm{des}} \sim \mathsf{SSR}\left(\dot{b},\dot{m},\dot{\Omega}\right), \tag{14}$$

with shadowing parameters scaled accordingly as

$$\dot{b}=P_{\mathrm{tx}}\cdot\mathrm{PL}^{-1}\cdot G_i(\phi_i,\theta_i)\cdot b, \tag{15}$$

$$\dot{m}=m, \tag{16}$$

$$\dot{\Omega}=P_{\mathrm{tx}}\cdot\mathrm{PL}^{-1}\cdot G_i(\phi_i,\theta_i)\cdot\Omega. \tag{17}$$

Notice that, when scaling the SSR random variable, the fading order m remains unchanged; only the average powers of the LOS and NLOS components have changed.

Perhaps more meaningful than desired signal power in dictating system performance is SNR, which is also a random variable and can be written as

$$\mathsf{SNR}=\frac{P_{\mathrm{des}}}{\sigma_{\mathrm{n}}^2}=\overline{\mathsf{SNR}}\cdot|h|^2, \tag{18}$$

where we use $\overline{\mathsf{SNR}}$ to denote the large-scale SNR without random channel variations as

$$\overline{\mathsf{SNR}}=\frac{P_{\mathrm{tx}}\cdot\mathrm{PL}^{-1}\cdot G_i(\phi_i,\theta_i)}{\sigma_{\mathrm{n}}^2}. \tag{19}$$

Since SNR is linearly related to $|h|^2$, Theorem 1 states that it follows an SSR distribution tied to that of the channel h as

$$\mathsf{SNR} \sim \mathsf{SSR}\left(\overline{\mathsf{SNR}}\cdot b,m,\overline{\mathsf{SNR}}\cdot\Omega\right). \tag{20}$$

In this setting, given the presence of multi-beam interference, SNR only partially dictates system performance. Nonetheless, it is important to realize that the distribution of SNR sets the upper bound on system performance. As such, under SR channels, it is essential that the system be designed so that $\overline{\mathsf{SNR}}$ is sufficiently high with an accordingly high probability for any user needing service. Note that this only depends on system parameters, channel conditions, and fading parameters, not the actual channel realization.

B. Interference Power and INR

Along with the desired signal power, the interference power is also a key indicator of system performance, especially in multi-beam satellite systems, where co-channel interference from neighboring spot beams can be difficult to avoid. Since interference from neighboring spot beams propagates along the same path to a ground user, the collective interference power can be expressed as a sum of correlated SSR random variables, which itself turns out to be an SSR random variable proportional to $|h|^2$, as we will see.

From (3), the total spot beam interference power $P_{\rm int}$ inflicted on a user served by the i-th spot beam is

$$P_{\rm int} = \sum_{j=1, j\neq i}^{N_{\rm B}} P_{\rm tx} \cdot {\rm PL}^{-1} \cdot G_j(\phi_j, \theta_j) \cdot |h|^2, \tag{21}$$

which depends on the channel gain $|h|^2$ and the gain of each interfering spot beam in the direction of the user. As with desired signal power, Theorem 1 states that interference power is an SSR random variable distributed as

$$P_{\rm int} \sim \mathsf{SSR}\big(\bar{b}, \bar{m}, \bar{\Omega}\big), \tag{22}$$

with shadowing parameters scaled as

$$\bar{b} = \sum_{j=1, j\neq i}^{N_{\rm B}} P_{\rm tx} \cdot {\rm PL}^{-1} \cdot G_j(\phi_j, \theta_j) \cdot b, \tag{23}$$

$$\bar{m} = m, \tag{24}$$

$$\bar{\Omega} = \sum_{j=1, j\neq i}^{N_{\rm B}} P_{\rm tx} \cdot {\rm PL}^{-1} \cdot G_j(\phi_j, \theta_j) \cdot \Omega. \tag{25}$$

INR is an important quantity for communication systems plagued by interference since it indicates if the system is noise-limited ($\mathsf{INR} \ll 0$ dB) or interference-limited ($\mathsf{INR} \gg 0$ dB). Like SNR, INR is linearly related to $|h|^2$ as

$$\mathsf{INR} = \frac{P_{\rm int}}{\sigma_{\rm n}^2} = \overline{\mathsf{INR}} \cdot |h|^2, \tag{26}$$

where $\overline{\mathsf{INR}}$ is the large-scale INR capturing the leakage of each interfering spot beam onto the ground user being served,

$$\overline{\mathsf{INR}} = \frac{P_{\rm tx} \cdot {\rm PL}^{-1} \cdot \sum_{j=1, j\neq i}^{N_{\rm B}} G_j(\phi_j, \theta_j)}{\sigma_{\rm n}^2}. \tag{27}$$

Theorem 1 straightforwardly describes INR as an SSR random variable distributed as

$$\mathsf{INR} \sim \mathsf{SSR}\big(\overline{\mathsf{INR}} \cdot b, m, \overline{\mathsf{INR}} \cdot \Omega\big). \tag{28}$$

Notice that $\overline{\mathsf{INR}}$ is solely a function of system parameters: transmit power, path loss, noise power, and the sum spot beam gain toward the ground user. This naturally introduces the challenge of cell planning and spot beam steering to mitigate the effects of interference (deliver a low $\overline{\mathsf{INR}}$) without degrading coverage. Although INR is a random variable, engineers can use $\overline{\mathsf{INR}}$ to ensure a given ground user sees below some level of interference with certain probability based on the SR channel statistics. As mentioned in the introduction, the beam gain observed by users on the ground is a function of the elevation angle of the satellite since the beam pattern distorts as it projects onto the surface of the Earth. Consequently, the satellite elevation angle adds to the complexity of cell planning and spot beam steering, which we investigate further in Section V.

C. SIR and SINR

The strength of a desired signal and that of interference are both useful metrics on their own, but combining the two provides truer indications of system performance. To begin, we consider SIR, that is the ratio of desired signal power to that of interference, which can in fact be written deterministically as

$$\mathsf{SIR} = \frac{P_{\rm des}}{P_{\rm int}} = \frac{\mathsf{SNR}}{\mathsf{INR}} = \frac{\overline{\mathsf{SNR}}}{\overline{\mathsf{INR}}} = \frac{G_i(\phi_i, \theta_i)}{\sum_{j=1, j\neq i}^{N_{\rm B}} G_j(\phi_j, \theta_j)}. \tag{29}$$

While desired signal power $P_{\rm des}$ and interference power $P_{\rm int}$ are both SSR random variables, it is important to note that they are fully correlated, both depending on the same random variable $|h|^2$. Recall, this is due to the fact that the stochastics seen by the signal of the i-th spot beam are also seen by the signals of the other spot beams, considering they propagate along the same path from the satellite to a given ground user. As a result, from (29), it is clear that SIR only depends on the position of the ground user and the steering directions of the $N_{\rm B}$ spot beams.

Unlike SIR, the SINR of the system is indeed a random variable defined as

$$\mathsf{SINR} = \frac{\mathsf{SNR}}{1 + \mathsf{INR}} = \frac{\overline{\mathsf{SNR}}}{\frac{1}{|h|^2} + \overline{\mathsf{INR}}} \leq \min\left(\mathsf{SNR}, \mathsf{SIR}\right),$$

which does not follow the SSR distribution and cannot be easily described statistically. However, by considering that SINR is upper-bounded by the minimum of SNR and SIR, useful results emerge. In noise-limited regimes (i.e., when $\overline{\mathsf{INR}}$ is low), SINR can be approximated by SNR, meaning it is approximately distributed as

$$\mathsf{SINR} \overset{\overline{\mathsf{INR}} \to 0}{\sim} \mathsf{SSR}\big(\overline{\mathsf{SNR}} \cdot b, m, \overline{\mathsf{SNR}} \cdot \Omega\big). \tag{30}$$

On the other hand, when interference-limited (i.e., when $\overline{\mathsf{INR}}$ is high), SINR is approximated by SIR, from which it follows that

$$\mathsf{SINR} \overset{\overline{\mathsf{INR}} \to \infty}{=} \mathsf{SIR}. \tag{31}$$

Notice that, while the true level of interference INR is a random variable, engineers can rely on $\overline{\mathsf{INR}}$—which is based system parameters—to gauge conditions where SINR can be approximated by SNR or SIR with certain probability. Additionally, since SINR is upper-bounded by these two quantities, engineers can potentially leverage the fact that SIR is deterministic for cell planning and to design beam steering solutions that ensure system design does not bottleneck performance, regardless of the channel realization. With key performance metrics characterized in this section, we evaluate their stochastics in the next section to facilitate statistical analyses of LEO satellite systems.

IV. A USEFUL APPROXIMATION ON FADING ORDER

In the previous section, we characterized downlink SNR, INR, SIR, and SINR of a multi-beam LEO system under the SR channel model. As mentioned in the introduction and made evident in the previous two sections, the statistics of SR and

$$\tilde{f}_Y(y) = \frac{1}{2b}\left(\frac{2bm}{2bm+\Omega}\right)^m \exp\left(-\frac{my}{2bm+\Omega}\right)\sum_{i=0}^{m-1}\frac{(m-1)!}{(m-1-i)!(i!)^2}\left(\frac{\Omega y}{2b(2bm+\Omega)}\right)^i \tag{32}$$

$$\tilde{F}_Y(y) = \left(\frac{2bm}{2bm+\Omega}\right)^{m-1}\sum_{i=0}^{m-1}\frac{(m-1)!}{(m-1-i)!(i!)^2}\left(\frac{\Omega}{2bm}\right)^i\left(i! - \gamma\left(i+1, \frac{my}{2bm+\Omega}\right)\right) \tag{33}$$

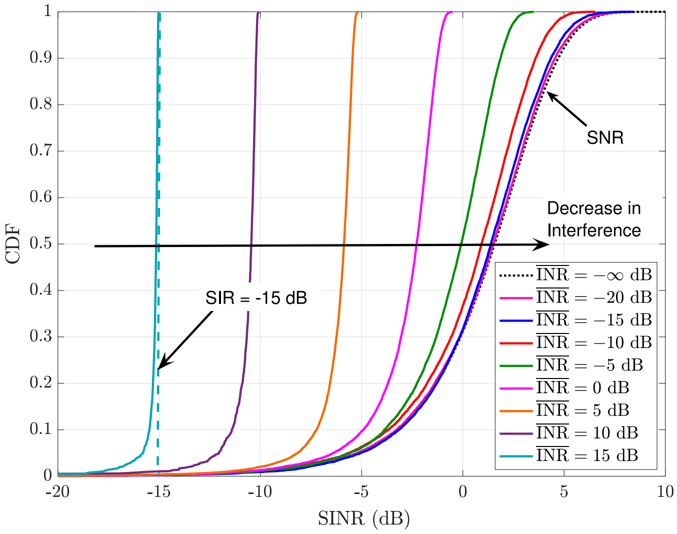

Fig. 2. The empirical CDF of SINR for various $\overline{\mathsf{INR}}$ where $\overline{\mathsf{SNR}} = 0$ dB and under light shadowing conditions (with integer m). The dotted black line where $\overline{\mathsf{INR}} = -\infty$ dB corresponds to the numerical CDF of SNR using (33), to which the distribution of SINR converges at low $\overline{\mathsf{INR}}$. At high $\overline{\mathsf{INR}}$, SINR converges to SIR, as evident by the increasing steepness of its CDF.

SSR random variables generally involve complex expressions and special functions, and their moments (e.g., expectation) cannot be stated concisely. This complicates statistical analysis of these key performance metrics. In this section, we show that statistically characterizing SR and SSR random variables simplifies when the fading order m of an SR random variable is an integer.

A. Probability of Outage

The probability that a desired signal's quality falls below some threshold—or the probability of *outage*—is an important quantity for evaluating and characterizing a communication system. For instance, in a noise-limited setting, the probability of SNR falling below some threshold is often a key metric of interest. As mentioned before, however, computing such generally involves infinite power series. To circumvent this, we present the following theorem and corollaries, which introduce a minor approximation on fading order that allows us to express the PDF and CDF of SSR random variables (such as SNR) in a closed-form without the use of infinite power series.

Theorem 2. *When the fading order m is an integer, the PDF of an SSR random variable $Y \sim \mathsf{SSR}(b, m, \Omega)$ as shown in* (8) *can be simplified as* (32)*, and its CDF as shown in* (9) *can be simplified as* (33)*, where $\gamma(a,x) = \int_0^x e^{-t}t^{a-1}\,dt$ is the unnormalized incomplete Gamma function [28].*

Proof. See Appendix B. ☐

With Theorem 2, we can represent the PDF and CDF of an SSR random variable under integer fading order m without an infinite power series in either expression. Using this, the probability of SNR outage is directly computed as

$$\mathbb{P}[\mathsf{SNR} \leq \beta] = \tilde{F}_Y\left(\beta \cdot \overline{\mathsf{SNR}}^{-1}\right), \tag{34}$$

where β is an SNR threshold. Although this SNR outage is an underestimate on the probability of SINR outage, it provides a closed-form expression for quantifying outage probability that offers convenience both numerically and analytically. This probability of SNR outage is especially useful in settings where interference is low, such as under less aggressive frequency reuse. Additionally, since $\mathsf{SINR} \leq \min(\mathsf{SNR}, \mathsf{SIR})$ and the fact that SIR is deterministic for a given design, engineers can calculate the probability that the system is not noise-limited by computing

$$\mathbb{P}[\mathsf{SNR} \leq \mathsf{SIR}] = \tilde{F}_Y\left(\mathsf{SIR} \cdot \overline{\mathsf{SNR}}^{-1}\right). \tag{35}$$

While this equality only holds when m is an integer, later in this section we show that rounding m to an integer often has minor impacts on the distribution, meaning it can often be reliably used to closely approximate the PDF and CDF of SSR random variables, even when m is not an integer.

To illustrate how the CDF of SNR in (33) can be used to approximate that of SINR, consider Fig. 2. For various $\overline{\mathsf{INR}}$, we draw realizations of $|h|^2 \sim \mathsf{SSR}(b, m, \Omega)$ under light shadowing (which we will describe in detail shortly [14], [25]) and calculate the resulting SINR as

$$\mathsf{SINR} = \frac{\overline{\mathsf{SNR}} \cdot |h|^2}{1 + \overline{\mathsf{INR}} \cdot |h|^2}, \tag{36}$$

where we fix $\overline{\mathsf{SNR}} = 0$ dB. We plot the empirical CDF of SINR and compare it against the CDF of $\mathsf{SNR} = \overline{\mathsf{SNR}} \cdot |h|^2$ based on (33). When $\overline{\mathsf{INR}}$ is sufficiently low (e.g., $\overline{\mathsf{INR}} \leq -15$ dB), the distribution of SNR reliably approximates that of SINR. Therefore, if a satellite system can estimate $\overline{\mathsf{SNR}}$ and $\overline{\mathsf{INR}}$, which are based solely on system parameters, and has an estimate of the SR channel statistics, it can obtain an approximate distribution of SINR, assuming $\overline{\mathsf{INR}}$ is sufficiently low. As remarked earlier, if $\overline{\mathsf{INR}}$ is sufficiently high, SIR is a good approximation of SINR, in which case it is deterministic based on beam steering and cell placement, as described by (29). This can be observed in Fig. 2 as the CDF of SINR trends toward $\mathsf{SIR} = -15$ dB at $\overline{\mathsf{INR}} = 15$ dB (recall, $\overline{\mathsf{SNR}} = 0$ dB in this example).

The complementary cumulative distribution function (CCDF) of INR can be derived straightforwardly using (33) as the probability that the INR exceeds a certain level δ as

$$\mathbb{P}[\mathsf{INR} \geq \delta] = 1 - \tilde{F}_Y\left(\delta \cdot \overline{\mathsf{INR}}^{-1}\right), \tag{37}$$

which can be used to determine if the system tends to be interference-limited or noise-limited.

B. Expected SNR and INR

In addition to probability of outage, it is also useful to examine the mean SNR and INR of a system. Recall, the mean of an SSR random variable is highly involved for general m [14]; the following corollary can be used to express it in an intuitive closed-form when the fading order m is an integer.

Corollary 2.1. *The mean of* $Y \sim \mathsf{SSR}(b, m, \Omega)$ *when* m *is an integer is*

$$\mathbb{E}[Y] = 2 \cdot b + \Omega. \tag{38}$$

Proof. See Appendix C. ☐

Corollary 2.2. *In the special case when* $Y \sim \mathsf{SSR}(b, m, \Omega)$ *with* $m = 1$*,* Y *follows the exponential distribution with PDF and CDF respectively as*

$$\tilde{f}_Y(y; b, 1, \Omega) = \frac{1}{2b + \Omega} \cdot \exp\left(-\frac{y}{2b + \Omega}\right), \tag{39}$$

$$\tilde{F}_Y(y; b, 1, \Omega) = 1 - \exp\left(-\frac{y}{2b + \Omega}\right). \tag{40}$$

The mean and variance of Y *are* $\mathbb{E}[Y] = 2 \cdot b + \Omega$ *and* $\mathbb{V}[Y] = \mathbb{E}[Y]^2$*, respectively.*

Using Corollary 2.1, the expected SNR and INR with integer fading order m are simply

$$\mathbb{E}[\mathsf{SNR}] = \overline{\mathsf{SNR}} \cdot (2 \cdot b + \Omega), \tag{41}$$

$$\mathbb{E}[\mathsf{INR}] = \overline{\mathsf{INR}} \cdot (2 \cdot b + \Omega). \tag{42}$$

These expected values are intuitively captured as the sum of the average powers of the LOS and NLOS components of the SR channel when m is an integer. For some $\overline{\mathsf{SNR}}$, $\overline{\mathsf{INR}}$, and channel parameters (b, Ω), engineers can gauge the expected SNR and INR for any integer m. Albeit limited, these quick calculations can be used by engineers to determine average performance of the system. For instance, engineers can gauge if a particular user will be interference-limited on average or not, based solely on $\overline{\mathsf{INR}}$—which depends only on system parameters—and an estimate of channel conditions (b, Ω).

C. Impact of Approximating Fading Order as an Integer

Theorem 2 and the consequent corollaries rely on the fading order m being an integer. In cases where m is not an integer, approximating it as such can facilitate statistical analyses without deviating significantly from the original distribution with non-integer m. In Fig. 3, we illustrate this with three different shadowing intensities [14], [25]: light, average, and heavy, which are tabulated in Table I and elaborated on in the next section. The PDFs of the three shadowing levels with their true m are shown as solid lines; markers indicate their counterparts with m rounded to the nearest integer. Notice that m varies from less than 1 to over 19, and each pair of distributions is extremely closely aligned—so much so that we have to use markers instead of separate lines to distinguish the two. With PDFs virtually identical for general m and integer m, it is guaranteed that their statistics also be closely aligned. It is important to note that the parameters (b, m, Ω) for these three shadowing levels were obtained by fitting the SR distribution to channel measurements [14], [25]. As such, one can reason that the effects of rounding m to the nearest integer are even less pronounced in practice, since any statistical model fitted to measurements will inherently not perfectly align with reality. Minute distributional differences invisible to the naked eye, therefore, are immaterial for most practical applications. With all this being said, we believe Theorem 2 and Corollary 2.1 can be used as fairly reliable and useful approximations for any SR distribution by rounding the fading order m to the nearest integer.

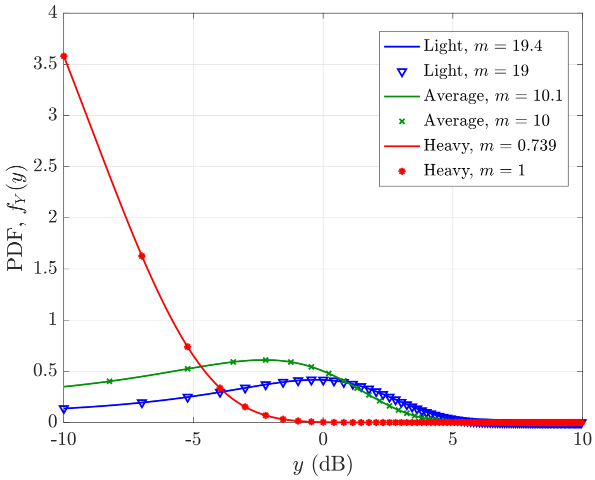

Fig. 3. The PDF of an SSR random variable Y with integer and non-integer fading order m for various levels of shadowing, as shown in Table I and fitted from measurements in [14], [25]. Even when rounding the fading order m to the nearest integer, the shadowing distributions remain virtually unchanged.

TABLE I
SSR PARAMETERS FITTED FROM MEASUREMENTS [14], [25].

Shadowing Level	Light	Average	Heavy
b	0.158	0.126	0.063
m	19.4	10.1	0.739
Ω	1.29	0.835	8.97×10^{-4}

V. Performance Evaluation of a Multi-Beam LEO Satellite System in Shadowed Rician Channels

In this section, we simulate a 20 GHz (Ka-band) multi-beam LEO satellite communication system and evaluate the impact various system parameters have on key performance metrics, namely SNR, INR, and SINR. A summary of parameters used for simulation is listed in Table II, most of which are based

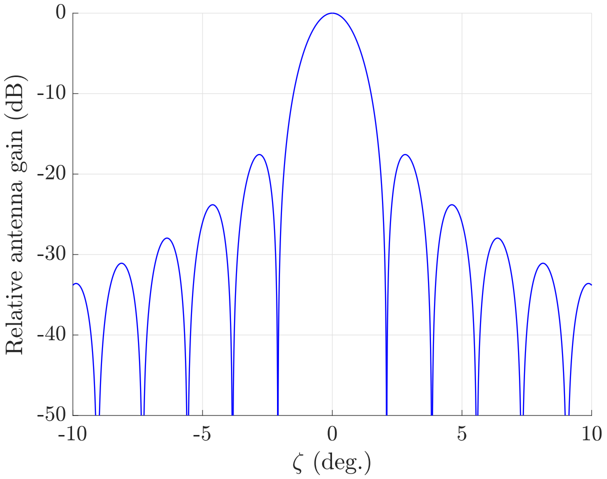

Fig. 4. Normalized beam pattern of each high-gain dish antenna onboard the satellite as a function of angle off boresight ζ.

TABLE II
SYSTEM SIMULATION PARAMETERS [31], [32].

Altitude (H)	600 km
Carrier frequency (f_c)	20 GHz
System bandwidth	400 MHz
Satellite transmit power	4 dBW/MHz
Maximum transmit beam gain	38.5 dBi
Ground user receiver type	VSAT
Maximum receive beam gain	39.7 dBi
Ground user noise figure	1.2 dB
Spotbeam cell boresight	Steered to the center of its cell
Cell radius	10 km
Number of spot beams (N_B)	19

on [31], [32] published by 3GPP. We simulate a satellite at an altitude of $H = 600$ km equipped with dish antennas creating $N_\mathrm{B} = 19$ spot beams, each steered toward the center of its cell on the ground. Cells are tessellated in a hexagonal fashion with a cell radius of 9.24 km. The gain delivered by the i-th spot beam to a user on the ground we model as a steerable dish antenna with gain pattern [31]

$$G_i(\phi,\theta) = \begin{cases} 1, & \zeta = 0^\circ \\ 4\left|\dfrac{J_1(ka\sin\zeta)}{ka\sin\zeta}\right|^2, & 0^\circ < |\zeta| \leq 90^\circ \end{cases} \tag{43}$$

where $\zeta = \arccos\left(\cos\phi \cdot \cos\theta\right)$ is the absolute angle off antenna boresight, $J_1(\cdot)$ is the first-order Bessel function of the first kind, a is the radius of the dish antenna, $k = 2\pi/\lambda$ is the wave number, and λ is the carrier wavelength. We model ground users as very small aperture terminals (VSAT) mounted on rooftops or vehicles with a maximum receive antenna gain of 39.7 dBi, a noise figure of 1.2 dB, and an antenna temperature of 150 K (i.e., $G/T = 15.9$ dB/K) [32]. For simplicity, we assume ground users track their serving satellite to offer maximum receive gain and are associated to cells based on their locations.

In real low-earth orbit (LEO) satellite systems, downlink signals experience significant Doppler effects due to the motion of satellites relative to the Earth. We do not directly incorporate these Doppler effects into our analysis for two main reasons. For one, desired and interference signals undergo the same Doppler effects since they originate from the same satellite. Secondly, it has been shown that Doppler effects can be effectively and reliably estimated and compensated for in real deployments [33], [34], especially when such systems have knowledge of satellite orbitals and ground user locations—which is often the case.

We consider SR channels with three levels of shadowing intensity—light, average, and heavy—whose parameters (b, m, Ω) are fitted from measurements in [14] and are shown in Table I. Users are randomly distributed on the ground and their channels are assumed to be independent and identically distributed. Each dish antenna onboard supplies 4 dBW/MHz of fixed transmit power. We simulate the system over a bandwidth of 400 MHz. Path loss is modeled as the combination of free-space path loss and atmospheric attenuation as [31]

$$\mathrm{PL}(d, f_\mathrm{c}, \epsilon) = \mathrm{PL}_\mathrm{FS}(d, f_c) + \mathrm{PL}_\mathrm{g}(f_c, \epsilon), \tag{44}$$

which is a function of propagation distance d, carrier frequency f_c, and satellite elevation angle ϵ. Here, free-space path loss (in dB) is modeled as [31]

$$\left[\mathrm{PL}_\mathrm{FS}(d, f_c)\right]_\mathrm{dB} = 32.45 + 20\log_{10}(f_\mathrm{c}) + 20\log_{10}(d), \tag{45}$$

which captures clutter loss and additional large-scale shadowing. Absorption by atmospheric gases is modeled as [35], [36]

$$\mathrm{PL}_\mathrm{g}(f_\mathrm{c}, \epsilon) = \frac{A_\mathrm{zen}(f_\mathrm{c})}{\sin\epsilon}, \tag{46}$$

where A_zen is a zenith attenuation given as $A_\mathrm{zen} = 0.9$ at a carrier frequency of $f_\mathrm{c} = 20$ GHz [36]. It is important to keep in mind throughout our results that quantities like SNR and INR would simply scale with arbitrary differences in large-scale terms such as path loss, noise power, or transmit power adaptation.

A. Effect of Elevation Angle

We begin our system evaluation by highlighting the effect of satellite elevation angle on the antenna gain delivered to ground users depending on their locations. In Fig. 5, the delivered beam gain of a single spot beam across multiple cells is presented when the beam is steered to the center cell at the origin. Thus, the maximum gain of 38.5 dB is delivered to the center of the centermost cell. The satellite's position and elevation are relative to the center of the centermost cell located at the origin. In the figure, blue circles/ellipses are created by the nulls of the beam in Fig. 4. The area inside the first null corresponds to the main lobe beam, and the areas between the nulls circles are due to side lobe leakage.

In practice, the transmit beam width and a cell radius are system design parameters which are carefully decided, taking into account the inter-cell interference and regional capacity of a system. The larger the cell radius, the less inter-cell interference per cell and the smaller the number of cells, which can lead to eventual capacity reduction. On the other hand, the wider the beam width, the more the inter-cell interference for a fixed cell radius.

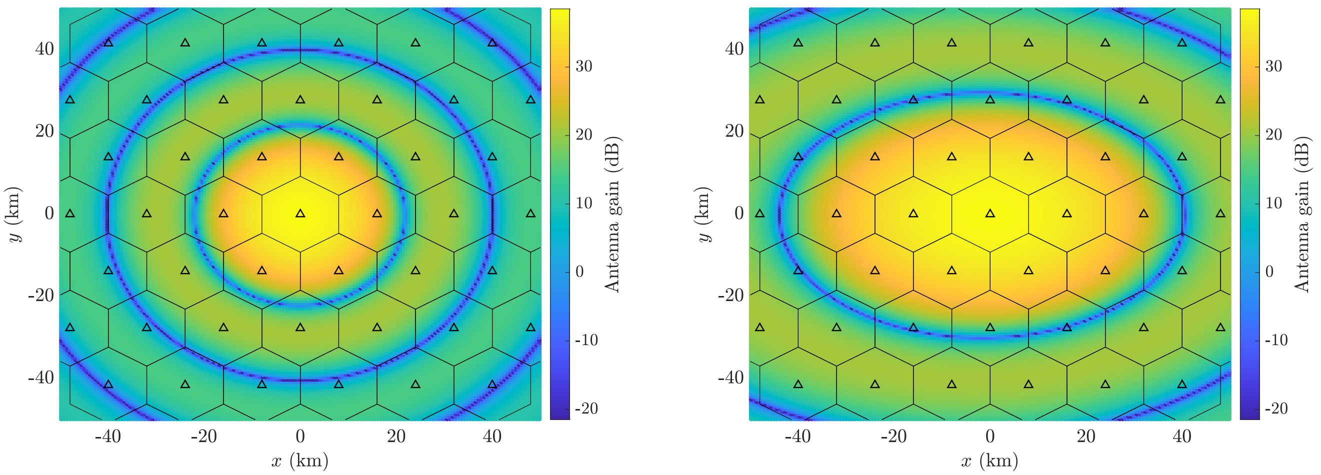

(a) Elevation of $\epsilon = 90°$.

(b) Elevation of $\epsilon = 45°$.

Fig. 5. Delivered gain of a spot beam over multiple hexagonal cells when the spot beam is steered to a center cell on the ground at $(x, y) = (0, 0)$ for elevations (a) $\epsilon = 90°$ and (b) $\epsilon = 45°$. The blue circles/ellipses are created by nulls of the beam as visible in Fig. 4. The area inside the first null corresponds to the main lobe beam, and the area between the first and the second nulls corresponds to the first side lobe. Triangles denote cell centers.

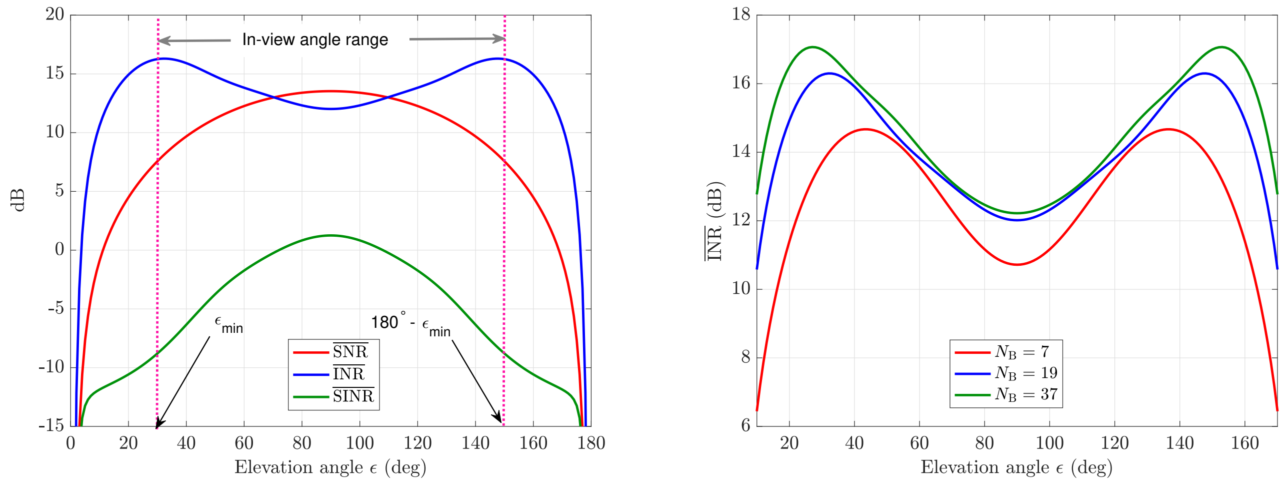

(a) $\overline{\text{SNR}}$, $\overline{\text{INR}}$, and $\overline{\text{SINR}}$ as a function of elevation angle.

(b) $\overline{\text{INR}}$ for various numbers of spot beams.

Fig. 6. (a) $\overline{\text{SNR}}$, $\overline{\text{INR}}$, and $\overline{\text{SINR}} = \overline{\text{SNR}}/(1 + \overline{\text{INR}})$ as a function of elevation angle for $N_{\text{B}} = 19$ spot beams. $\overline{\text{SNR}}$ and $\overline{\text{SINR}}$ are monotonic above and below $\epsilon = 90°$, whereas $\overline{\text{INR}}$ is not. (b) $\overline{\text{INR}}$ as a function of elevation angle for various numbers of spot beams N_{B}. The level of interference begins to saturate as the number of beams increases, since the main lobes of spot beams are the most significant contributors of interference.

In Fig. 5a, the satellite is directly overhead the origin at an elevation of $\epsilon = 90°$. The observed spot beam gain is circularly symmetric around the center of the centermost cell where its energy is concentrated the most. It shows that the main lobe energy arrives with significant gain at the centermost cell and its surrounding six cells, which we refer to as *first-tier* cells. The first side lobe inflicts substantially onto the *second-tier* cells surrounding the first-tier cells, with gain at most around 18 dB below the main lobe.

At an elevation of 45°, the satellite is closer to the horizon. The observed spot beam gain becomes more elliptical as it projects onto the surface of the Earth as shown in Fig. 5b. Consequently, the beam gain elongates in the x dimension and tightens along the y dimension. The main lobe delivers significant gain over a wider area compared to Fig. 5a, and the nulls create elliptical boundaries. The main lobe inflicts energy across the first-tier cells, along with several second-tier cells as well, which worsens interference, as we will see.

Fig. 6a shows how $\overline{\text{SNR}}$, $\overline{\text{INR}}$, and $\overline{\text{SINR}}$ change with elevation angle ϵ when the total number of spot beams is $N_{\text{B}} = 19$, where we define $\overline{\text{SINR}} = \overline{\text{SNR}}/(1 + \overline{\text{INR}})$. Intuitively, these plots are symmetric about an elevation of $\epsilon = 90°$. The $\overline{\text{SNR}}$ is maximized when the satellite is overhead at $\epsilon = 90°$. The $\overline{\text{INR}}$ also rises as the elevation angle increases from 0° to a certain degree, which we refer to as the *minimum elevation angle* ϵ_{min}, representing the point at which interference starts to diminish. After the satellite passes the minimum elevation angle ϵ_{min}, the $\overline{\text{INR}}$ falls until it moves overhead to $\epsilon = 90°$.

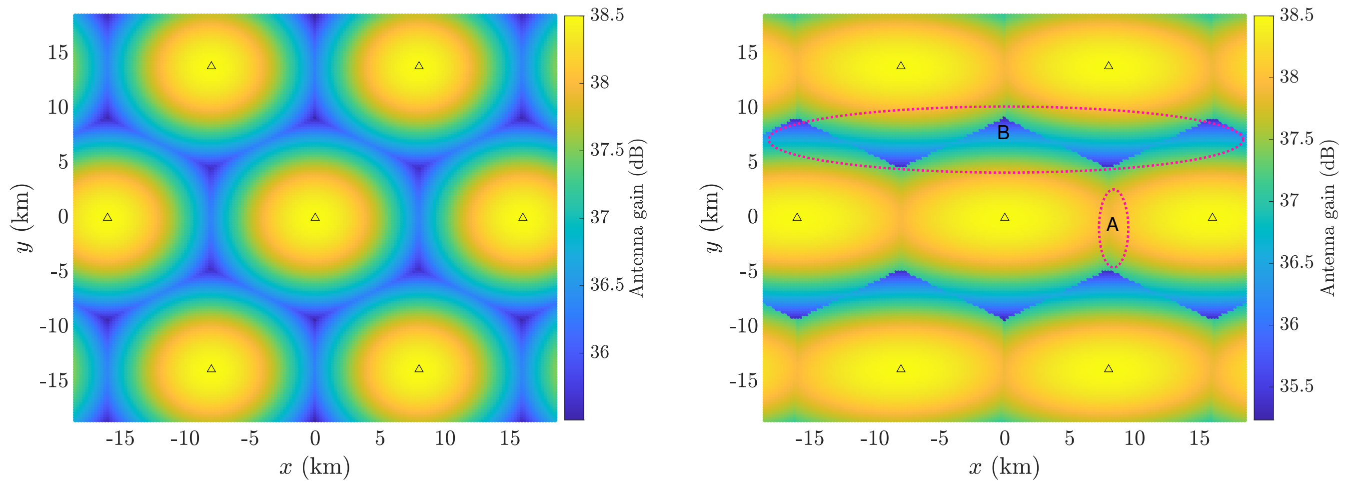

(a) Elevation of $\epsilon = 90^\circ$.

(b) Elevation of $\epsilon = 45^\circ$.

Fig. 7. Delivered antenna gain as a function of ground user position for a satellite elevation angle of (a) $\epsilon = 90^\circ$ and (b) $\epsilon = 45^\circ$. Delivered beam gain distorts to a more elliptical shape at lower elevations, leading to less defined cell boundaries. Triangles denote cell centers. At an elevation of $\epsilon = 45^\circ$, ground users at the cell edge in region A enjoy 2–3 dB higher beam gain than cell-edge users in region B, courtesy of the distorted beam shape.

We define the *in-view angle range* as

$$\{\epsilon : \epsilon_{\min} \leq \epsilon \leq 180^\circ - \epsilon_{\min}\}. \tag{47}$$

Signals at extreme elevation angles out of the in-view angle range experience substantial path loss due to extended path distance by (2), and therefore, we observe very low $\overline{\mathsf{SNR}}$ and $\overline{\mathsf{INR}}$ at elevations within this range.

In Fig. 6b, we plot the $\overline{\mathsf{INR}}$ observed at the cell center as a function of elevation angle for various numbers of spot beams N_{B}. Notice that $\epsilon_{\min}$ differs with N_{B}. Within the in-view angle range, $\overline{\mathsf{INR}}$ is minimized at $\epsilon = 90^\circ$, increases as the elevation falls from overhead, and reaches its maximum at $\epsilon = \epsilon_{\min}$ for each N_{B}. As we increase the number of spot beams N_{B} from 7 to 19, we observe an increase in $\overline{\mathsf{INR}}$. However, this increase in $\overline{\mathsf{INR}}$ diminishes when increasing from $N_{\mathrm{B}} = 19$ to $N_{\mathrm{B}} = 37$. In other words, as a satellite employs more spot beams to serve more cells on the ground, interference increases but eventually saturates, attributed to the fact that the main lobe and first side lobe of neighboring beams are the most significant sources of interference, as shown in Fig. 5a.

In Fig. 7, we show the delivered desired beam gain for each ground cell as a function of ground users' location relative to its serving cell center. In Fig. 7a, the satellite is directly overhead at an elevation of $\epsilon = 90^\circ$. Plotting the observed antenna gain as a function of ground user location reveals the hexagonal arrangement of our cells; shown here are the six first-tier cells surrounding the centermost cell. In Fig. 7a, when $\epsilon = 90^\circ$, the observed spot beam gain within each cell is nearly circular, which leads to well-defined cell boundaries. Maximum delivered transmit beam gain is around 38.5 dB with cell-edge users losing around 3 dB of gain for this particular cell radius. At an elevation of 90°, a user's distance from the center of its cell is a good indicator of the antenna gain it enjoys. At an elevation of 45°, cell boundaries are no longer as well-defined and user distance from the center of the cell is no longer a clear indicator of delivered beam gain, as shown in Fig. 7b—a notable difference from terrestrial cellular systems. For instance, users in region A, enjoy near-maximal beam gain even though they are at the cell edge. Users in region B, also at the cell edge, see around 2–3 dB less beam gain. All these takeaways can be extrapolated for elevations between 45° and 90° and, through symmetry, beyond to 135°.

B. SNR Distribution

Now, instead of considering delivered beam gain, which is solely a function of cell placement and user location, we examine SNR as a function of user location in the presence of light shadowing (see Table I) in Fig. 8. We again consider elevations of $\epsilon = 90^\circ$ and $\epsilon = 45^\circ$ in Fig. 8a and Fig. 8b, respectively. The beam patterns observed before are apparent here at a high level, as trends in SNR follow those seen in Fig. 7. Users in region A tend to enjoy higher SNRs than those in region B. In both cases, SNR tends to be higher near the center of each cell, with best-case users enjoying SNRs from around 15 dB up to even 20 dB. Notice that SNRs observed at $\epsilon = 90^\circ$ are around 2–3 dB higher than those at $\epsilon = 45^\circ$; this is attributed to increased slant distance d (and hence path loss) at lower elevation angles. Some users enjoy SNR gains courtesy of constructive fading, particularly useful to those that observe lower $\overline{\mathsf{SNR}}$ at the cell edge, but more prominently, we see that shadowing can cause deep fades, regardless of user location. Naturally, since users close to the center of the cell enjoy higher $\overline{\mathsf{SNR}}$, they are more robust to these deep fades but are not exempt from such.

In Fig. 9, we plot the CDF of SNR populated by (33) (solid lines) and by simulations for various shadowing levels and elevation angles $\epsilon = 90^\circ$ (dashed lines) and $\epsilon = 45^\circ$ (dotted lines). The distributions based on simulation are taken across users within the center cell and across channel realizations. For the solid lines based on (33), the distribution plotted is

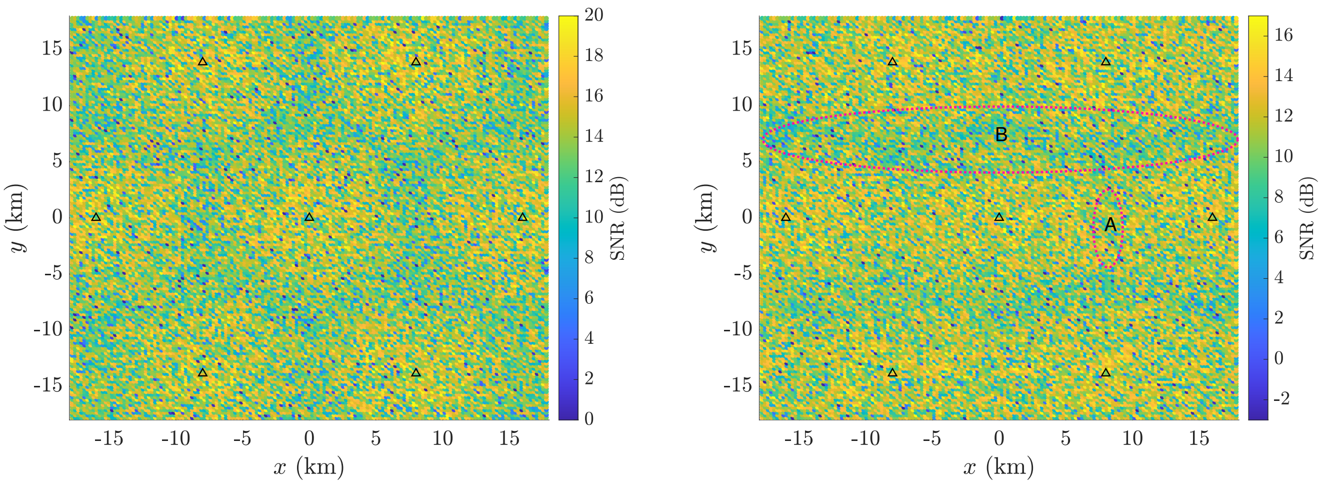

(a) Elevation of $\epsilon = 90°$.

(b) Elevation of $\epsilon = 45°$.

Fig. 8. Received SNR as a function of user location under light shadowing for a satellite elevation angle of (a) $\epsilon = 90°$ and (b) $\epsilon = 45°$. User location is a good indicator for trends in SNR, but SR channel stochastics can lead to deep fades even near the center of the cell. Triangles denote cell centers.

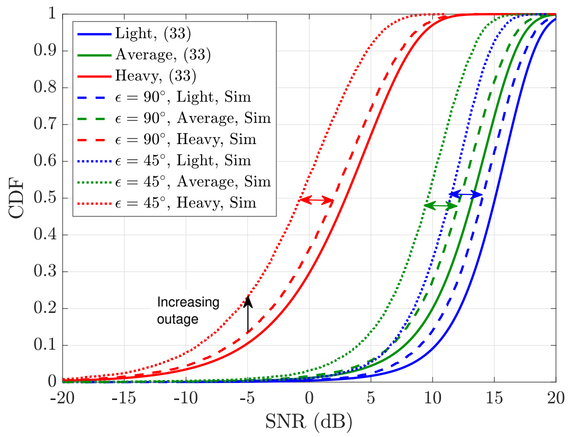

Fig. 9. The CDFs of SNR generated by (33) and by simulations for various shadowing levels and elevations of $\epsilon = 90°$ and $\epsilon = 45°$.

with $\overline{\mathsf{SNR}} = 13.5$ dB, seen by a user at the center of the cell when the satellite is directly overhead at $\epsilon = 90°$.

For each shadowing level, a gap of approximately 1 dB exists between the distributions obtained from (33) (solid lines) and simulations (dashed lines) at $\epsilon = 90°$. This gap grows to about 3 dB at an elevation of $\epsilon = 45°$. These gaps are due to the fact that delivered beam gain to the user at the center of the cell is always higher than that of users across the cell, with a gap up to about 3 dB. However, since performance at the center of the cell provides some measure of performance across the cell, engineers can use (33) to gauge cell-wide performance once $\overline{\mathsf{SNR}}$ and channel parameters are estimated.

Light shadowing conditions produce the highest SNR distribution, with median users enjoying around $\mathsf{SNR} = 14$ dB at $\epsilon = 90°$ and just over $\mathsf{SNR} = 11$ dB at $\epsilon = 45°$. Worst-case users in light shadowing can suffer from deep fades, resulting in SNRs falling well below 5 dB at both elevations. As shadowing intensifies, the SNR distribution shifts leftward—a shift of about 12 dB in median from light to heavy shadowing—from which the shadowing level can severely impact performance. Heavier shadowing produces a heavier lower tail and more variance overall. Since the effects of shadowing are independent of those due to elevation angle, there is a consistent 2–3 dB gap in distribution between $\epsilon = 90°$ and $\epsilon = 45°$ across all three shadowing levels, caused by the $\overline{\mathsf{SNR}}$ gap between these two elevations as shown in Fig. 6a.

Fig. 9 also provides insight on how shadowing and elevation impacts SNR outage probability. For example, under an SNR threshold of -5 dB, the outage probability is almost zero in the case of light and average shadowing but increases significantly in the case of a heavy shadowing environment. Along with heavier shadowing, lowering the elevation angle from 90° to 45° increases the outage probability—an increase of about 10% under heavy shadowing.

C. INR Distribution

Having considered SNR, we now turn our attention to examining INR in a similar manner. In Fig. 10, we plot a realization of INR as a function of ground user location for elevations of 90° and 45° under light shadowing. At an elevation of 90°, INR typically ranges from around 10 dB to upwards of 20 dB. Inverse to SNR, INR tends to increase as users approach the cell edge, where spot beam overlap is at its peak. At an elevation of 45°, INR increases overall due to the distorted beam gain. Interestingly, we see that INR tends to be higher in region B compared to region A—opposite of what was observed with SNR. This can be best explained by considering users located precisely at points A and B. A user at point A sees one dominant interferer (the spot beam serving the cell to the right of the center cell), whereas a user at point B sees the combination of two nearby interferers (the spot beams serving the two cells above the center cell). Notice that the beam gains at these locations in Fig. 7b differ by less than

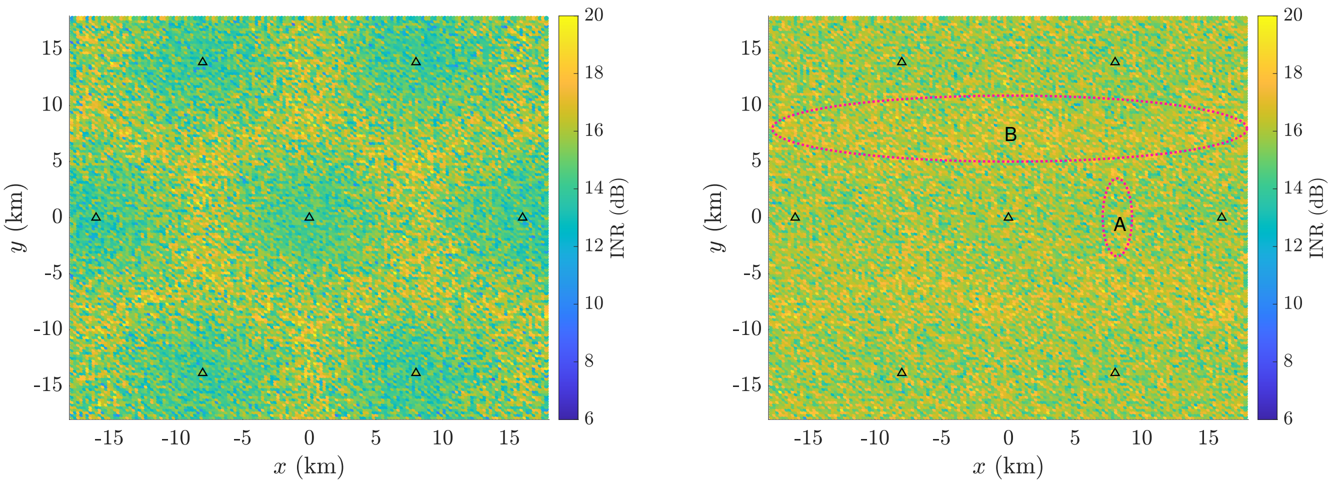

(a) Elevation of $\epsilon = 90°$.

(b) Elevation of $\epsilon = 45°$.

Fig. 10. INR as a function of ground user location under light shadowing for a satellite elevation angle of (a) $\epsilon = 90°$ and (b) $\epsilon = 45°$. At the elevation angle below 90°, users in region B tend to see more interference than those in region A at elevations below 90°. Triangles denote cell centers.

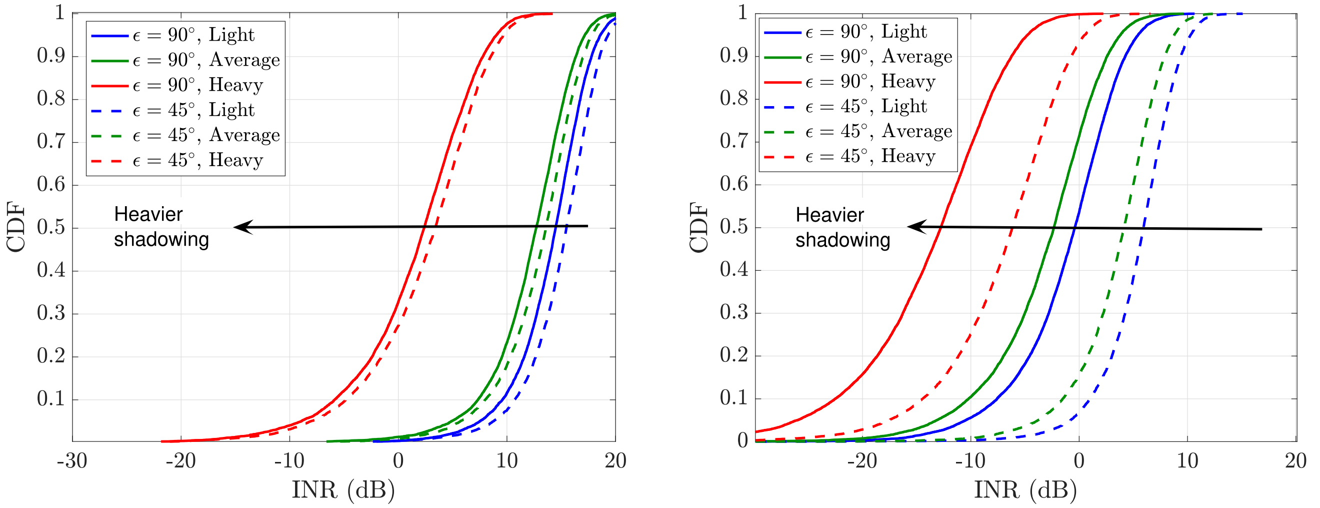

(a) Frequency reuse factor of one.

(b) Frequency reuse factor of three.

Fig. 11. The CDF of INR for various shadowing levels at elevations of 90° and 45° with (a) a frequency reuse factor of one and (b) a frequency reuse factor of three. As the frequency reuse factor increases, elevation angle plays a greater role in the degree of interference seen by users.

3 dB, meaning doubling the number of dominant interferers at point B will result in its total interference exceeding that at point A.

Thus far, we have assumed a frequency reuse factor of one where all cells use the same frequency resources. Unlike SNR, INR is dictated by the particular frequency reuse factor since inter-beam interference reduces with increased separation between beams operating on the same spectrum. In Fig. 11a, we plot the CDF of INR for various levels of shadowing and for elevations $\epsilon = 90°$ and $\epsilon = 45°$, where the frequency reuse factor is one. This is the CDF of INR across ground user locations in the center cell in Fig. 10. In Fig. 11b, we plot that of Fig. 11a except with a frequency reuse factor of three, where any three cells adjacent to one another use non-overlapping frequency resources.

Fig. 11a illustrates that increasing the shadowing level reduces interference between spot beams since the interference power is proportional to the channel gain. It also shows that elevation plays a minor role in overall distribution—approximately a mere 1 dB increase from 90° to 45°. With a frequency reuse factor of three, on the other hand, different conclusions are drawn. As with a frequency reuse factor of one, overall interference reduces as shadowing intensifies with a frequency reuse factor of three. Naturally, interference decreases as the frequency reuse factor is increased from one to three—here, by about 15 dB. Notice that, with a frequency reuse factor of one, the system tends to be interference-limited (INR $>$ 0 dB), except on occasion under heavy shadowing.

With a frequency reuse factor of three, however, the system is more often noise-limited. This is attributed to the fact that leakage from the main lobe of spot beams onto adjacent cells is the dominant source of interference. When a satellite is

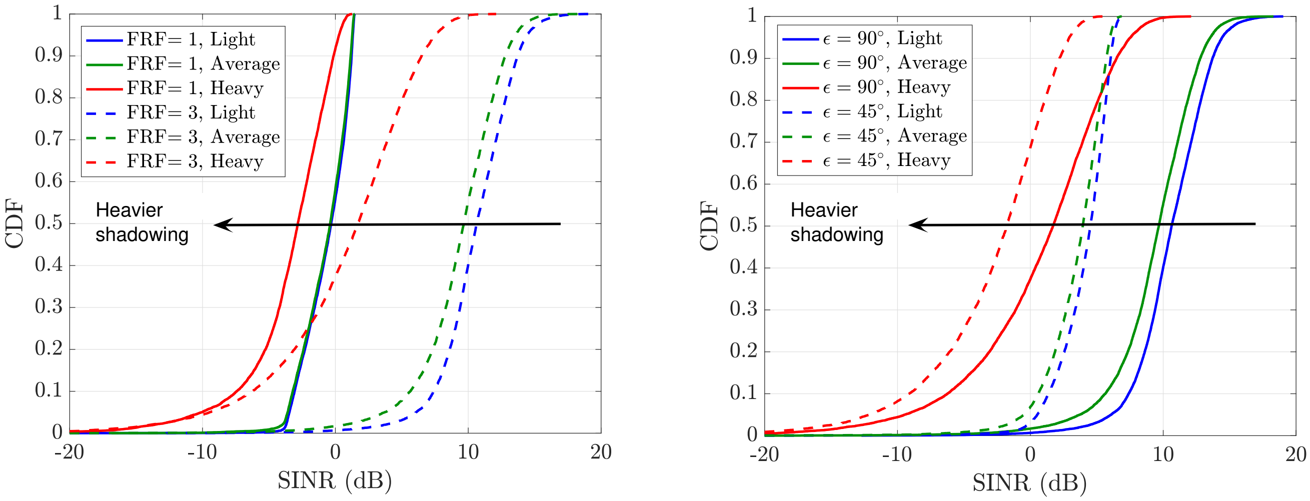

(a) Elevation of $\epsilon = 90^\circ$.

(b) Frequency reuse factor of three.

Fig. 12. (a) The CDF of SINR under various shadowing levels for frequency reuse factors (shown as FRF) of one and three at an elevation of $\epsilon = 90^\circ$. (b) The CDF of SINR under various shadowing levels for a frequency reuse factor of three at various elevation angles.

overhead at an elevation of 90°, even light shadowing has a median INR just less than 0 dB. As the elevation drops to 45°, the INR distribution shifts rightward by about 6–7 dB, pushing the system to more often be interference-limited, as the main lobe elongates as illustrated in Fig. 5b. In other words, under light and average shadowing, an elevation of 45° typically leads to strong interference, even with a frequency reuse factor of three. Increasing the frequency reuse further would reduce interference but should be done so carefully to balance overall system performance.

This shift in limitedness as the satellite traverses across the sky motivates the design of adaptive LEO satellite systems, which may sway from interference-limited to noise-limited and back to interference-limited within a minute or two. In addition, these results emphasize that elevation, shadowing intensity, and frequency reuse should be taken into account holistically when evaluating the presence of spot beam interference and its distribution.

D. SINR Distribution

To conclude our numerical evaluation, we now examine downlink SINR, the chief metric quantifying system performance. In Fig. 12a, we show the CDF of SINR under various shadowing levels for frequency reuse factors of one and three at an elevation of 90°. Under a frequency reuse factor of one, all three shadowing levels yield SINR distributions that lay largely below 0 dB and with heavy lower tails due to severe spot beam interference. System performance under heavy shadowing is particularly poor as over 90% of users experience $\mathsf{SINR} \leq 0$ dB. The SINR distribution in light and average shadowing takes an interesting shape—a consequence of the system being primarily interference-limited, as noted before from Fig. 11a. Light and average shadowing yield nearly identical distributions. This is due to the fact that both yield interference-limited conditions, meaning SINR can be approximated as SIR, which is independent of the shadowing realization, as evidenced by (31). The sharp bend in these distributions can similarly be seen in Fig. 2 at high $\overline{\mathsf{INR}}$. Interference reduces as the frequency reuse factor is increased from one to three, improving median SINR by 5 dB under heavy shadowing and by over 10 dB under average or light shadowing. This reduction in spot beam interference pushes the SINR distribution to levels that can sustain communication and with less severe lower tails.

In Fig. 12b, we fix the frequency reuse factor to three and highlight the effects of elevation angle. As the satellite traverses from 90° to 45°, the SINR distribution shifts leftward—a result of SNR decreasing and INR increasing as remarked before. Under average and light shadowing, users see a reduction of around 6 dB in median SINR at 45° and, in heavy shadowing, experience $\mathsf{SINR} \leq 0$ dB 70% of the time. As emphasized before, system performance can vary notably as the satellite traverses across the sky, largely due to the distorted beam shape observed by users on the ground. This can lead to lower SNRs and higher interference, resulting in lower SINRs. System performance improves as the satellite comes overhead and will degrade as it nears the horizon. With all of this happening over the course of a minute or two, appropriate measures should be taken to dynamically adapt the system based on satellite position and shadowing conditions.

E. Summary

For convenience, below we summarize the key conclusions drawn from this numerical evaluation:

- The main lobes of neighboring spot beams are the dominant source of significant interference. Consequently, as the number of spot beams increases, the amount of interference increases but saturates.
- At elevations other than 90°, delivered beam gain is no longer circular, and hence distance from the center of the cell is not a clear indicator of received signal quality (i.e., SINR).

- SNRs observed at an elevation angle $\epsilon = 45^\circ$ are around 3 dB lower than those at an elevation angle $\epsilon = 90^\circ$ due to increased path distance. The gap in SNR distribution between elevations of 90° and 45° remains constant over any shadowing level since the effects of shadowing are independent of those due to elevation angle.
- As shadowing intensifies, both SNR and INR distributions shift leftward as they are proportional to the channel gain.
- Interference tends to be higher when the satellite is not directly overhead due to distorted/elliptical beam patterns.
- With a frequency reuse factor of one, elevation angle plays a minor role in INR. With a frequency reuse factor of three, the system can swing between noise-limited and interference-limited regimes depending on elevation angle.
- System performance tends to improve as the satellite comes overhead and degrades as it nears the horizon. Thus, appropriate measures should be taken to dynamically adapt the system based on satellite position and shadowing conditions.

VI. CONCLUSION AND FUTURE DIRECTIONS

LEO satellite communication systems are evolving into a more prominent role connecting people and machines around the globe. In this work, we analyzed multi-beam LEO satellite systems under the measurement-backed SR channel model. We derived key performance metrics including SNR, INR, SIR, and SINR and provided a statistical characterization of each under SR channels. Our analyses and derivations can be useful tools for the statistical evaluation and the design of LEO satellite systems. To facilitate this, we showed that rounding the SR fading order to an integer can simplify expressions of PDF, CDF, and expectation, allowing researchers to more straightforwardly calculate probability of outage, for instance. Then, we conducted a performance of evaluation of a 20 GHz multi-beam LEO system through simulation with practical system parameters and realistic antenna, channel, and path loss models. Our results highlighted the effects of elevation angle, shadowing conditions, and frequency reuse on SNR, INR, and SINR, which motivates the need for frequency reuse factors above one and for systems that can adapt to varying conditions as the satellite traverses across the sky along its orbit.

Future work that can capitalize on the derivations and insights herein include optimal cell planning and spot beam design, along with other means to manage interference, potentially using machine learning. Naturally, strategic handover and scheduling will be paramount in successfully overcoming the constant orbiting of satellite base stations. Finally, statistically characterizing entire networks of LEO satellites will be an essential stride toward validating the efficacy of these new wireless systems and the role they will play in next-generation connectivity.

REFERENCES

[1] E. Kim, I. P. Roberts, P. A. Iannucci, and J. G. Andrews, “Downlink analysis of LEO multi-beam satellite communication in Shadowed Rician channels,” in *Proc. IEEE GLOBECOM*, Dec. 2021, pp. 01–06.

[2] SpaceX. Non-geostationary satellite system attachment a technical information to supplement schedule S. Federal Communications Commission, Washington DC, USA, 2021. [Online]. Available: https://fcc.report/IBFS/SAT-MOD-20181108-00083/1569860.pdf

[3] J. Hindin. Technical Appendix, Application of Kuiper systems LLC for authority to launch and operate a non-geostationary satellite orbit system in Ka-band frequencies. Federal Communications Commission, Washington DC, USA, 2019. [Online]. Available: https://docs.fcc.gov/public/attachments/FCC-20-102A1.pdf

[4] B. Palacin, N. J. G. Fonseca, M. Romier, R. Contreres, J.-C. Angevain, G. Toso, and C. Mangenot, “Multibeam antennas for very high throughput satellites in Europe: Technologies and trends,” in *Proc. Eur. Conf. Antennas Propag.*, Mar. 2017, pp. 2413–2417.

[5] Y. Rahmat-Samii and A. C. Densmore, “Technology trends and challenges of antennas for satellite communication systems,” *IEEE Trans. Antennas Propag.*, vol. 63, no. 4, pp. 1191–1204, Apr. 2015.

[6] J. M. Montero, A. M. Ocampo, and N. J. G. Fonseca, “C-band multiple beam antennas for communication satellites,” *IEEE Trans. Antennas Propag.*, vol. 63, no. 4, pp. 1263–1275, Apr. 2015.

[7] W. Zheng, J. Li, Y. Luo, J. Chen, and J. Wu, “Multi-user interference pre-cancellation for downlink signals of multi-beam satellite system,” in *Proc. CECNet.*, Nov. 2013, pp. 415–418.

[8] E. Lutz, “Towards the Terabit/s satellite - interference issues in the user link,” *Intl. J. Sat. Commun. Net.*, vol. 34, pp. 461–482, Jun. 2015.

[9] L. Cottatellucci, M. Debbah, G. Gallinaro, R. Müller, and M. Neri, “Interference mitigation techniques for broadband satellite systems,” in *Proc. AIAA ICSSC*, vol. 1, Jun. 2006, pp. 1–13.

[10] C. Windpassinger, R. F. H. Fischer, T. Vencel, and J. B. Huber, “Precoding in multiantenna and multiuser communications,” *IEEE Trans. Wireless Commun.*, vol. 3, no. 4, pp. 1305–1316, Jul. 2004.

[11] Y. Su, Y. Liu, Y. Zhou, J. Yuan, H. Cao, and J. Shi, “Broadband LEO satellite communications: Architectures and key technologies,” *IEEE Wireless Commun.*, vol. 26, no. 2, pp. 55–61, Apr. 2019.

[12] S. Chen, S. Sun, and S. Kang, “System integration of terrestrial mobile communication and satellite communication —the trends, challenges and key technologies in B5G and 6G,” *China Commun.*, vol. 17, no. 12, pp. 156–171, Dec. 2020.

[13] X. Lin, S. Cioni, G. Charbit, N. Chuberre, S. Hellsten, and J.-F. Boutillon, “On the path to 6G: Embracing the next wave of low Earth orbit satellite access,” *IEEE Commun. Mag.*, vol. 59, no. 12, pp. 36–42, Dec. 2021.

[14] A. Abdi, W. C. Lau, M. Alouini, and M. Kaveh, “A new simple model for land mobile satellite channels: first- and second-order statistics,” *IEEE Trans. Wireless Commun.*, vol. 2, no. 3, pp. 519–528, May 2003.

[15] A. M.K., “Imperfect CSI based maximal ratio combining in Shadowed-Rician fading land mobile satellite channels,” in *National Conf. Commun. (NCC)*, Mar. 2015, pp. 1–6.

[16] D.-H. Jung, J.-G. Ryu, W.-J. Byun, and J. Choi, “Performance analysis of satellite communication system under the Shadowed-Rician fading: A stochastic geometry approach,” *IEEE Trans. Commun.*, vol. 70, no. 4, pp. 2707–2721, Apr. 2022.

[17] G. Alfano and A. De Maio, “Sum of squared Shadowed-Rice random variables and its application to communication systems performance prediction,” *IEEE Trans. Wireless Commun.*, vol. 6, no. 10, pp. 3540–3545, Oct. 2007.

[18] M. C. Clemente and J. F. Paris, “Closed-form statistics for sum of squared Rician shadowed variates and its application,” *Electronics Lett.*, vol. 50, pp. 120–121, Jan. 2014.

[19] N. I. Miridakis, D. D. Vergados, and A. Michalas, “Dual-hop communication over a satellite relay and Shadowed Rician channels,” *IEEE Trans. Veh. Technol*, vol. 64, no. 9, pp. 4031–4040, Sep. 2015.

[20] S. Sreng, B. Escrig, and M. Boucheret, “Exact outage probability of a hybrid satellite terrestrial cooperative system with best relay selection,” in *2013 IEEE ICC*, Jun. 2013, pp. 4520–4524.

[21] J. Sedin, L. Feltrin, and X. Lin, “Throughput and capacity evaluation of 5G New Radio non-terrestrial networks with LEO satellites,” in *Proc. IEEE GLOBECOM*, Dec. 2020, pp. 1–6.

[22] S. Xia, Q. Jiang, C. Zou, and G. Li, “Beam coverage comparison of LEO satellite systems based on user diversification,” *IEEE Access*, vol. 7, pp. 181 656–181 667, Dec. 2019.

[23] I. del Portillo Barrios, B. Cameron, and E. Crawley, “A technical comparison of three low Earth orbit satellite constellation systems to provide global broadband,” *ACTA Astronautica*, vol. 159, Mar. 2019.

[24] O. B. Osoro and E. J. Oughton, “A techno-economic framework for satellite networks applied to low Earth orbit constellations: Assessing Starlink, OneWeb and Kuiper,” *IEEE Access*, vol. 9, pp. 141 611–141 625, Oct. 2021.

[25] C. Loo, “A statistical model for a land mobile satellite link,” *IEEE Trans. Veh. Technol.*, vol. 34, no. 3, pp. 122–127, Aug. 1985.

[26] C. Loo and J. S. Butterworth, “Land mobile satellite channel measurements and modeling,” in *Proc. IEEE*, vol. 86, no. 7, Jul. 1998, pp. 1442–1463.

[27] S. Gradshteyn and I. M. Ryzhik, *Table of Integrals, Series, and Products*. New York: Academic, 2000.

[28] M. Abramowitz and I. A. Stegun, *Handbook of Mathematical Functions*. New York: Dover Publications, 1994.

[29] J. F. Paris, “Closed-form expressions for Rician shadowed cumulative distribution function,” *Electronics Lett.*, vol. 46, pp. 952–953, Jul. 2010.

[30] Y. A. Brychkov and N. Saad, “Some formulas for the Appell function $\mathcal{F}_1(a,b,b';c;w,z)$,” *Integral Transforms and Special Functions*, vol. 23, no. 11, pp. 793–802, Nov. 2012.

[31] 3GPP, “Technical Report 38.811, Study on New Radio (NR) to support non-terrestrial networks (NTN),” Jul. 2020.

[32] 3GPP, “Technical Report 38.821, Solutions for New Radio (NR) to support non-terrestrial networks (NTN),” Dec. 2019.

[33] M. Arti, “Two-way satellite relaying with estimated channel gains,” *IEEE Trans. Commun.*, vol. 64, no. 7, pp. 2808–2820, Jul. 2016.

[34] T. Darwish, G. K. Kurt, H. Yanikomeroglu, M. Bellemare, and G. Lamontagne, “Leo satellites in 5G and beyond networks: A review from a standardization perspective,” *IEEE Access*, vol. 10, pp. 35 040–35 060, 2022.

[35] Recommendation ITU-R P 618-13, “Propagation data and prediction methods required for the design of Earth-space telecommunication systems,” Dec. 2017.

[36] Recommendation ITU-R P 676-11, “Attenuation by atmospheric gases,” Sep. 2016.

APPENDIX A
PROOF OF THEOREM 1

The PDF of Y is obtained by plugging in $x = \sqrt{\frac{y}{k}}$ into $f_Y(y) = f_X(x)\frac{dx}{dy}$, leading to

$$\begin{aligned} f_Y(y) &= f_{X=|h|}\left(x=\sqrt{\frac{y}{k}}; b,m,\Omega\right)\frac{dx}{dy} && (48)\\ &= \frac{1}{2kb}\left(\frac{2kbm}{2kbm+k\Omega}\right)^m \exp\left(-\frac{y}{2kb}\right)\\ &\quad \times {}_1\mathcal{F}_1\left(m,1,\frac{k\Omega}{2kb(2kbm+k\Omega)}y\right) && (49)\\ &= f_{|h|^2}(y;kb,m,k\Omega), && (50) \end{aligned}$$

where $f_{|h|}(\cdot)$ and $f_{|h|^2}(\cdot)$ are given in (5) and (8), respectively.

APPENDIX B
PROOF OF THEOREM 2

Rewriting the confluent hypergeometric function for integer $m \geq 1$ as a polynomial via Kummer’s transform [28], we have

$$\begin{aligned} {}_1\mathcal{F}_1(m,1,x) &= e^x\,{}_1\mathcal{F}_1(1-m,1,-x) && (51)\\ &= e^x \sum_{i=0}^{m-1} \frac{(m-1)!\cdot x^i}{(m-1-i)!\cdot i!\cdot(1)_i}, && (52) \end{aligned}$$

which, along with algebra, yields (32). Using (32), the CDF of Y is obtained as

$$\begin{aligned} \tilde{F}_Y(y) &= \int_0^y \tilde{f}_Y(t)dt && (53)\\ &= \frac{1}{2b}\left(\frac{2bm}{2bm+\Omega}\right)^m \int_0^y \exp\left(-\frac{m}{2bm+\Omega}t\right)\\ &\quad \times \sum_{i=0}^{m-1}\frac{(m-1)!}{(m-1-i)!(i!)^2}\left(\frac{\Omega t}{2b(2bm+\Omega)}\right)^i dt && (54)\\ &= \frac{1}{2b}\left(\frac{2bm}{2bm+\Omega}\right)^m \sum_{i=0}^{m-1}\frac{(m-1)!}{(m-1-i)!(i!)^2}\\ &\quad \times \left(\frac{\Omega}{2b(2bm+\Omega)}\right)^i \int_0^y \exp\left(-\frac{m}{2bm+\Omega}t\right)t^i dt && (55)\\ &= \left(\frac{2bm}{2bm+\Omega}\right)^{m-1} \sum_{i=0}^{m-1}\frac{(m-1)!}{(m-1-i)!(i!)^2}\left(\frac{\Omega}{2bm}\right)^i\\ &\quad \times \left(i! - \gamma\left(i+1,\frac{my}{2bm+\Omega}\right)\right). && (56) \end{aligned}$$

APPENDIX C
PROOF OF COROLLARY 2.1

The expected value of Y is derived as

$$\begin{aligned} \mathbb{E}[Y] &= \int_0^\infty y\tilde{f}_Y(y)dy && (57)\\ &= \frac{1}{2b}\left(\frac{2bm}{2bm+\Omega}\right)^m \sum_{i=0}^{m-1}\frac{(m-1)!}{(m-1-i)!(i!)^2}\\ &\quad \times \left(\frac{\Omega}{2b(2bm+\Omega)}\right)^i \int_0^\infty \exp\left(-\frac{my}{2bm+\Omega}\right)y^{i+1}dy && (58)\\ &\overset{\text{(a)}}{=} \frac{1}{2b}\left(\frac{2bm}{2bm+\Omega}\right)^m \left(\frac{2bm+\Omega}{m}\right)^2\\ &\quad \times \sum_{i=0}^{m-1}\frac{(m-1)!(i+1)}{(m-1-i)!i!}\left(\frac{\Omega}{2bm}\right)^i && (59)\\ &\overset{\text{(b)}}{=} (2\cdot b+\Omega), && (60) \end{aligned}$$

where (a) is obtained using [27]

$$\int_0^\infty z^i e^{-\mu z}dz = i!\mu^{-i-1}, \qquad (61)$$

and (b) is derived using

$$\begin{aligned} \sum_{i=0}^{m-1}\frac{(m-1)!(i+1)}{(m-1-i)!i!}\left(\frac{\Omega}{2bm}\right)^i &= \sum_{i=0}^{m-1}\binom{m-1}{i}(i+1)\left(\frac{\Omega}{2bm}\right)^i && (62)\\ &= \left(1+\frac{\Omega}{2bm}\right)^{m-2}\left(1+\frac{\Omega}{2b}\right). && (63) \end{aligned}$$

Eunsun Kim (Student Member, IEEE) received the B.S. and M.S. degrees in Electrical Engineering from Yonsei University in South Korea. She was with LG Electronics from 2005 to 2018, where she worked on the technical development of cellular and Wi-Fi communication systems and was involved in standardization efforts with numerous technical contributions on LTE/LTE-A/5G NR in the 3GPP RAN1 group and on TV white space PHY/MAC layer technologies in the IEEE 802.11af task group.

She is currently pursuing her Ph.D. degree in Electrical and Computer Engineering at the University of Texas at Austin. Her technical interests include satellite communication systems with mega-constellations, the coexistence of satellite communication systems, and the application of machine learning algorithms in wireless communications. She has worked with Samsung Research America and Amazon's Project Kuiper on state-of-the-art non-geostationary satellite communication systems.

Ian P. Roberts (Member, IEEE) received the B.S. degree in Electrical Engineering from Missouri University of Science and Technology and the M.S. and Ph.D. degrees in Electrical and Computer Engineering from the University of Texas at Austin, where he was a National Science Foundation Graduate Research Fellow with the Wireless Networking and Communications Group. He has industry experience developing and prototyping wireless technologies at AT&T Labs, Amazon, GenXComm (startup), and Sandia National Labs.

He is currently an Assistant Professor at UCLA in the Department of Electrical and Computer Engineering. His research interests are in the theory and implementation of millimeter wave systems, full-duplex, and other next-generation technologies for wireless communication and sensing. He received the 2023 Andrea Goldsmith Young Scholars Award from the Communication Theory Technical Committee of the IEEE Communications Society.

Jeffrey G. Andrews (Fellow, IEEE) received the B.S. in Engineering with High Distinction from Harvey Mudd College, and the M.S. and Ph.D. in Electrical Engineering from Stanford University. He is the Truchard Family Chair in Engineering at the University of Texas at Austin where he is Director of the 6G@UT research center. He developed CDMA systems at Qualcomm, and has served as a consultant to Samsung, Nokia, Qualcomm, Apple, Verizon, AT&T, Intel, Microsoft, Sprint, and NASA. He is co-author of the books *Fundamentals of WiMAX* (Prentice-Hall, 2007) and *Fundamentals of LTE* (Prentice-Hall, 2010). He was the Editor-in-Chief of the IEEE TRANSACTIONS ON WIRELESS COMMUNICATIONS from 2014-2016, and is the founding Chair of the Steering Committee for the IEEE JOURNAL ON SELECTED AREAS IN INFORMATION THEORY (2018-23), and was Chair of the IEEE Communication Theory Technical Committee (2021-22).

Dr. Andrews is an IEEE Fellow and ISI Highly Cited Researcher and has been co-recipient of 16 best paper awards including the 2016 IEEE Communications Society & Information Theory Society Joint Paper Award, the 2014 IEEE Stephen O. Rice Prize, the 2014 and 2018 IEEE Leonard G. Abraham Prize, the 2011 and 2016 IEEE Heinrich Hertz Prize, and the 2010 IEEE ComSoc Best Tutorial Paper Award. His other major awards include the 2015 Terman Award, the NSF CAREER Award, the 2021 Gordon Lepley Memorial Teaching Award at UT Austin, the 2021 IEEE ComSoc Joe LoCicero Service Award, the 2019 IEEE Wireless Communications Technical Committee Recognition Award, and the 2019 IEEE Kiyo Tomiyasu Award, which is an IEEE Technical Field Award.